DOI: 10.13009/EUCASS2017-607

On-board DA-based state estimation algorithm for spacecraft relative navigation

Francesco Cavenago⋆†*, Pierluigi Di Lizia*⋆*, Mauro Massari*⋆*, and Alexander Wittig*⋆⋆

⋆*Politecnico di Milano,Via La Masa 34, 20156 Milano, Italy*
francesco.cavenago@polimi.it · pierluigi.dilizia@polimi.it · mauro.massari@polimi.it

⋆⋆*European Space Agency (ESA/ESTEC), Keplerlaan 1, 2201 AZ Noordwijk, Netherlands*
alexander.wittig@esa.int

†Corresponding author

Abstract

This paper analyzes the real-time relative pose estimation and attitude prediction of a tumbling target spacecraft through a high-order numerical extended Kalman filter based on differential algebra. In particular, linear and nonlinear algorithms are developed and implemented on a BeagleBone Black platform, as representative of the limited computational capability available on onboard processors. The performance are assessed varying measurement acquisition frequency and processor clock frequency, and considering various levels of uncertainties. Moreover, a comparison among the different orders of the filter is carried out.

1. Introduction

Active debris removal (ADR) missions have gained increasing importance inside the space community due to the necessity of reducing the number of debris jeopardizing the operative satellites. In this context, autonomous guidance, navigation and control (GNC) plays a fundamental role in the problem of rendezvous with an uncooperative target. Especially, the estimation of the relative pose and the prediction of the attitude of the target are crucial for safe proximity operations.[14]

To deal with estimation problems, many filtering techniques have been developed. At present time, one of the most exploited estimation algorithm is the extended Kalman filter[8] (EKF). The EKF is based on the main idea of linearizing the equations of motion and the measurement equations via first-order Taylor expansions around the current mean and covariance. In some cases, however, the linear assumption may fail due to the nature of the dynamics or the number of available measurements, leading to inaccurate realization of the local motion. Therefore, alternative methods capable of accounting for system nonlinearity must be used. A different approach is the unscented Kalman filter[5,6] (UKF). This technique is based on the unscented transformation, which does not contain any linearization, and thus provides superior performance with respect to the EKF in highly nonlinear situations. However, the UKF is often slightly slower than the EKF. Conversely, Park and Scheeres[9,10] proposed a nonlinear filter named high-order numerical extended Kalman filter (HNEKF), which describes the local nonlinear motion by solving for higher-order Taylor series and maps the initial uncertainties. Since the prediction steps rely on a fully nonlinear mapping of the mean and covariance, this method turns out to be more accurate than the EKF. However, the HNEKF is numerically quite intensive due to the required derivation of the so-called higher-order tensors.

Later, the HNEKF was derived exploiting differential algebra (DA) techniques,[11] which significantly simplify the process, and applied to orbit determination problems.[13] Indeed, in the DA framework, the Taylor expansion of the phase flow is automatically available once the spacecraft dynamics is integrated and thus the need to write and integrate high-order variational equations is completely avoided. Despite the evident advantages, the DA approach is not free of drawbacks. More specifically, the approach relies on Taylor expansions and, thus, the problem to be dealt with must be well behaved. In addition, the computational burden associated to the calculation of the polynomials quickly increases with the order, and this could limit the current applicability of DA-based HNEKF for onboard applications.

The aim of this work is to assess the performance and onboard applicability of the DA-based HNEKF algorithm with the target application of estimating the relative pose between two spacecraft during a rendezvous maneuver. For

DOI: 10.13009/EUCASS2017-607

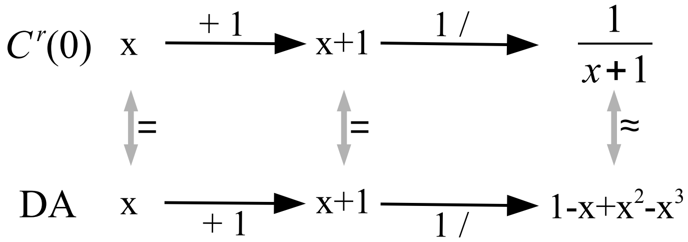

Figure 1: Evaluation of the expression $1/(1 + x)$ in $C^r(0)$ and DA arithmetic.

this purpose, linear and nonlinear algorithms are developed in the DA framework and implemented on a BeagleBone Black platform, as representative of the limited performance available on onboard processors.

The paper is organized as follows. First, an introduction to DA is given and the derivation of the DA-based HNEKF is explained. Then, a comparison among different orders of the filter is carried out. Afterwards, the considered relative pose estimation problem is introduced and the dynamics model is developed. Finally, the performance of the filters are assessed through numerical simulations.

2. Differential algebra

Differential Algebra techniques allow solving analytical problems through an algebraic approach.[2] Similar to the computer representation of real numbers as Floating Point (FP) numbers, DA allows the representation and manipulation of functions on a computer. Each sufficiently often differentiable function f is represented by its Taylor expansion around an expansion point truncated at an arbitrary finite order. Without loss of generality, we choose 0 as the expansion point. Algebraic operations on the space of truncated Taylor polynomials are defined such that they approximate the operations on the function space $C^r(0)$ of r times differentiable functions at 0. More specifically, each operation is defined to result in the truncated Taylor expansion of the correct result computed on the function space $C^r(0)$. This yields the so-called Truncated Power Series Algebra (TPSA).[1]

To illustrate the process, consider Fig. 1. The expression $1/(x + 1)$ is evaluated once in $C^r(0)$ (top) and then in DA with truncation order 3. Starting with the identity function x, we add one to arrive at the function $x + 1$, the representation of which is fully accurate in DA as it is a polynomial of order 1. Continuing the evaluation the multiplicative inversion is performed, resulting in the function $1/(1 + x)$ in $C^r(0)$. As this function is not a polynomial any more, it is automatically approximated in DA arithmetic by its truncated Taylor expansion around 0, given by $1 - x + x^2 - x^3$. Note that, by definition of the DA operations, the diagram for each single operation commutes. That is to say the same result is reached by first Taylor expanding a $C^r(0)$ function (moving from the top to the bottom of the diagram) and then performing the DA operation (moving from left to right), or by first performing the $C^r(0)$ operation and then Taylor expanding the result.

In addition to algebraic operations, the DA framework can be endowed with natural differentiation and integration operators, completing the structure of a differential algebra. Intrinsic functions, such as trigonometric and exponential functions, are built from elementary algebraic operations.[2] This way, Taylor expansions of arbitrary sufficiently smooth functions given by some closed-form expression can be computed fully algebraically in a computer environment. An implementation of such DA computer routines is available in the software DACE 2.0, which is used to implement the algorithm presented in this paper.

An important application of DA in engineering applications is the expansion of the flow $\varphi(t; x_0)$ of an Ordinary Differential Equation (ODE) to arbitrary order with respect to initial conditions, integration times and system parameters. The following is a short summary of the underlying concept. For a more complete introduction to DA, as well as a fully worked out illustrative example of a DA based ODE integrator using a simple Euler step, see.[13]

Consider the initial value problem

$$\begin{cases} \dot{x} = f(x, t) \\ x(t_0) = x_0, \end{cases} \tag{1}$$

and its associated flow $\varphi(t; x_0)$. By means of classical numerical integration schemes, such as Runge-Kutta or multistep methods, it is possible to compute the orbit of a single initial condition x_0 using floating point arithmetic on a computer. Starting instead from the DA representation of an initial condition x_0, and performing all operations in the numerical integration scheme in DA arithmetic, DA allows propagating the Taylor expansion of the flow around x_0 forward in time, up to the desired final time t_f, yielding a polynomial expansion of $\varphi(t_f; x_0 + \delta x_0)$ up to arbitrary order.

DOI: 10.13009/EUCASS2017-607

The conversion of standard explicit integration schemes to their DA counterparts is rather straightforward. One simply replaces all operations performed during the execution of the scheme by the corresponding DA operations. Step size control and error estimates are performed only on the constant part of the polynomial, i.e. the reference trajectory of the expansion point. The result is an automatic Taylor expansion of the result of the numerical method (i.e. the numerical approximation to the flow) with respect to any quantity that was initially set to a DA value.

The main advantage of the DA-based approach is that there is no need to derive, implement and integrate variational equations in order to obtain high-order expansions of the flow. As this is achieved by merely replacing algebraic operations on floating-point numbers by DA operations, the method is inherently ODE independent. Furthermore, an efficient implementation of DA such as the DACE 2.0 package, allows us to obtain high-order expansions with limited computational time.

3. High-order extended Kalman filter

This section is devoted to introduce the algorithm of the high-order DA-based HNEKF and to provide a first assessment of its performance. The equations of motion and measurement equations describing a generic dynamic system are as follows:

$$\begin{aligned} \boldsymbol{x}_{k+1} &= \boldsymbol{\Phi}(t_{k+1}; \boldsymbol{x}_k, t_k) + \boldsymbol{w}_k, \\ z_{k+1} &= \boldsymbol{h}(\boldsymbol{x}_{k+1}, t_{k+1}) + \boldsymbol{v}_{k+1}, \end{aligned} \tag{2}$$

where $\boldsymbol{x}_k$ is the m-dimensional vector of state, $\boldsymbol{w}_k$ is the process noise perturbing the state, z_k is the n-dimensional vector of actual measurements, $\boldsymbol{h}$ is the measurement function, and $\boldsymbol{v}_{k+1}$ is the measurement noise characterizing the observation error. The process noise and the measurement noise are assumed to be uncorrelated, that is, $E\{\boldsymbol{v}_i\ \boldsymbol{w}_j^T\} = 0$, with the autocorrelations $E\{\boldsymbol{w}_i\ \boldsymbol{w}_j^T\} = \boldsymbol{Q}_i\delta_{ij}$ and $E\{\boldsymbol{v}_i\ \boldsymbol{v}_j^T\} = \boldsymbol{R}_i\delta_{ij}$ for all discrete time indexes i and j.

Starting from the general theory of state estimation, HNEKF sequentially estimate the spacecraft state and the associated uncertainty by incorporating system nonlinearity in terms of higher-order Taylor expansions and relying on the assumption that uncertainties can be described using Gaussian statistics.

3.1 The DA-based HNEKF

Consider the system model equations (2). The filtering process can be summarized as follows:

1. *Prediction step*: at time t_{k+1}, the mean and covariance of the state vector, $\boldsymbol{m}_{k+1}^-$ and P_{k+1}^-, and the mean of the measurements, $\boldsymbol{n}_{k+1}^-$, are estimated as:

$$\begin{aligned} m_{k+1,i}^- &= E\{\Phi_i(t_{k+1}; \boldsymbol{x}_k, t_k) + w_{k,i}\} \\ P_{k+1,ij}^- &= E\{[\Phi_i(t_{k+1}; \boldsymbol{x}_k, t_k) - m_{k+1,i}^- + w_{k,i}][\Phi_j(t_{k+1}; \boldsymbol{x}_k, t_k) - m_{k+1,j}^- + w_{k,j}]\} \\ n_{k+1,p}^- &= E\{h_p(\boldsymbol{x}_{k+1}, t_{k+1}) + v_{k+1,p}\}, \end{aligned} \tag{3}$$

   where $i, j = 1, ..., m$, $p = 1, ..., n$, $E\{\}$ denotes the expectation operator, and $m_{k+1,i}^-$, $P_{k+1,ij}^-$ and $n_{k+1,l}^-$ are the components of $\boldsymbol{m}_{k+1}^-$, P_{k+1}^-, and $\boldsymbol{n}_{k+1}^-$ respectively;

2. *Update step*: the new measurements acquired at time t_{k+1}, z_{k+1}, are incorporated into the updated estimate of the state vector and covariance matrix as follows:

$$\begin{aligned} P_{k+1,pq}^{zz} &= E\{[h_p(\boldsymbol{x}_{k+1}, t_{k+1}) - n_{k+1,p}^- + v_{k+1,p}][h_p(\boldsymbol{x}_{k+1}, t_{k+1}) - n_{k+1,q}^- + v_{k+1,p}]\} \\ P_{k+1,ip}^{xz} &= E\{[\Phi_i(t_{k+1}; \boldsymbol{x}_k, t_k) - m_{k+1,i}^- + w_{k,i}][h_p(\boldsymbol{x}_{k+1}, t_{k+1}) - n_{k+1,p}^- + v_{k+1,p}]\} \\ K_{k+1} &= P_{k+1}^{xz}(P_{k+1}^{zz})^{-1} \\ \boldsymbol{m}_{k+1}^+ &= \boldsymbol{m}_{k+1}^- + K_{k+1}(z_{k+1} - \boldsymbol{n}_{k+1}^-) \\ P_{k+1}^+ &= P_{k+1}^- - K_{k+1}P_{k+1}^{zz}K_{k+1}^T, \end{aligned} \tag{4}$$

   where $q = 1, ..., n$, K_{k+1} is the Kalman gain matrix, P_{k+1}^{xz} is the cross-covariance matrix of the state and the measurement, and P_{k+1}^{zz} is the covariance matrix of the measurements.

The DA implementation of the HNEKF relies on the fact that DA can easily provide the arbitrary order Taylor expansion of both $\boldsymbol{\Phi}$ and $\boldsymbol{h}$ in Eq. (2). Thus, the arbitrary order expansion of the equations of motion and measurement

DOI: 10.13009/EUCASS2017-607

equations can be easily written, and component-wise reads:

$$
\begin{aligned}
x_{k+1,i} &= \Phi_i(t_{k+1}; \boldsymbol{m}_k^+, t_k) + \sum_{r=1}^{v} \frac{1}{r!} \Phi^{i,\gamma_1 \dots \gamma_r}_{(t_{k+1},t_k)} \delta x^{\gamma_1}_{k,1} \dots \delta x^{\gamma_r}_{k,m} + w_{k,i}, \\
z_{k+1,p} &= h_p(\boldsymbol{\Phi}(t_{k+1}; \boldsymbol{m}_k^+, t_k), t_{k+1}) + \sum_{r=1}^{v} \frac{1}{r!} h^{p,\gamma_1 \dots \gamma_r}_{(t_{k+1},t_k)} \delta x^{\gamma_1}_{k,1} \dots \delta x^{\gamma_r}_{k,m} + v_{k+1,p},
\end{aligned}
\tag{5}
$$

where v is the order of the expansion, $\gamma_i \in \{1, ..., m\}$, $\Phi^{i,\gamma_1 \dots \gamma_r}_{(t_{k+1},t_k)}$ includes the higher-order partials of the solution flow, which map the deviations at time k to time $k+1$, and $h^{p,\gamma_1 \dots \gamma_r}_{(t_{k+1},t_k)}$ includes the higher-order partials of the measurement function. Both $\Phi^{i,\gamma_1 \dots \gamma_r}_{(t_{k+1},t_k)}$ and $h^{p,\gamma_1 \dots \gamma_r}_{(t_{k+1},t_k)}$ are obtained by integrating the equations of motion and evaluating the measurement equations in the DA framework.

The Taylor polynomials of Eq. (5) can be inserted into Eqs. (3) and (4) to obtain the steps of the high-order extended Kalman filter:

1. *Prediction step*: at time t_{k+1}, the mean and covariance of the state vector, $\boldsymbol{m}^-_{k+1}$ and P^-_{k+1}, and the mean of the measurements, $\boldsymbol{n}^-_{k+1}$, are estimated as:

$$
\begin{aligned}
m^-_{k+1,i} &= \Phi_i(t_{k+1}; \boldsymbol{m}_k^+, t_k) + \sum_{r=1}^{v} \frac{1}{r!} \Phi^{i,\gamma_1 \dots \gamma_r}_{(t_{k+1},t_k)} E\{\delta x^{\gamma_1}_{k,1} \dots \delta x^{\gamma_r}_{k,m}\} \\
P^-_{k+1,ij} &= \sum_{r=1}^{v} \sum_{s=1}^{v} \frac{1}{r!s!} \Phi^{i,\gamma_1 \dots \gamma_r}_{(t_{k+1},t_k)} \Phi^{j,\xi_1 \dots \xi_s}_{(t_{k+1},t_k)} E\{\delta x^{\gamma_1}_{k,1} \dots \delta x^{\gamma_r}_{k,m} \delta x^{\xi_1}_{k,1} \dots \delta x^{\xi_s}_{k,m}\} + \\
&\quad -\delta m^i_{k+1} \delta m^j_{k+1} + Q^{ij}_k \\
n^-_{k+1,p} &= h_p(\boldsymbol{\Phi}(t_{k+1}; \boldsymbol{m}_k^+, t_k), t_{k+1}) + \sum_{r=1}^{v} \frac{1}{r!} h^{p,\gamma_1 \dots \gamma_r}_{(t_{k+1},t_k)} E\{\delta x^{\gamma_1}_{k,1} \dots \delta x^{\gamma_r}_{k,m}\},
\end{aligned}
\tag{6}
$$

   where $\xi_i \in \{1, ..., m\}$ and $\delta m^i_{k+1} = \Phi_i(t_{k+1}; \boldsymbol{m}_k^+, t_k) - m^-_{k+1,i}$;

2. *Update step*: the new measurements acquired at time t_{k+1}, z_{k+1}, are incorporated into the updated estimate of the state vector and covariance matrix as follows:

$$
\begin{aligned}
P^{zz}_{k+1,pq} &= \sum_{r=1}^{v} \sum_{s=1}^{v} \frac{1}{r!s!} h^{p,\gamma_1 \dots \gamma_r}_{(t_{k+1},t_k)} h^{q,\xi_1 \dots \xi_s}_{(t_{k+1},t_k)} E\{\delta x^{\gamma_1}_{k,1} \dots \delta x^{\gamma_r}_{k,m} \delta x^{\xi_1}_{k,1} \dots \delta x^{\xi_s}_{k,m}\} + \\
&\quad -\delta n^p_{k+1} \delta n^q_{k+1} + R^{pq}_{k+1} \\
P^{xz}_{k+1,ip} &= \sum_{r=1}^{v} \sum_{s=1}^{v} \frac{1}{r!s!} \Phi^{i,\gamma_1 \dots \gamma_r}_{(t_{k+1},t_k)} h^{p,\xi_1 \dots \xi_s}_{(t_{k+1},t_k)} E\{\delta x^{\gamma_1}_{k,1} \dots \delta x^{\gamma_r}_{k} \delta x^{\xi_1}_{k,m} \dots \delta x^{\xi_s}_{k}\} + \\
&\quad -\delta m^i_{k+1} \delta n^p_{k+1} \\
K_{k+1} &= P^{xz}_{k+1} (P^{zz}_{k+1})^{-1} \\
\boldsymbol{m}^+_{k+1} &= \boldsymbol{m}^-_{k+1} + K_{k+1}(z_{k+1} - \boldsymbol{n}^-_{k+1}) \\
P^+_{k+1} &= P^-_{k+1} - K_{k+1} P^{zz}_{k+1} K^T_{k+1},
\end{aligned}
\tag{7}
$$

   where $\delta n^p_{k+1} = h_p(\boldsymbol{\Phi}(t_{k+1}; \boldsymbol{m}_k^+, t_k), t_{k+1}) - n^-_{k+1,p}$.

If the case of variables with Gaussian random distributions is considered, the higher-order moments $E\{\delta x^{\gamma_1}_k \dots \delta x^{\gamma_p}_k\}$ can be completely described by the first two moments (i.e., mean and covariance), and can be easily computed in terms of the covariance matrix using Isserlis' formula on the monomials of the Taylor polynomial.[4] It is worth to stress that, in the DA framework, the high-order partials integration, required by standard HNEKF, is completely avoided.

3.2 Order comparison

Before applying the DA-based HNEKF to the relative pose estimation problem, the effects of considering high-order expansion of the dynamic flow in the extended Kalman filter is discussed.

Consider the illustrative example of a spacecraft at the pericenter of an elliptical orbit of eccentricity $e = 0.5$, moving in Keplerian dynamics. Assume the lengths are scaled by the orbit pericenter r_p and the time by $\sqrt{r_p^3/\mu}$. Thus, the nominal initial state is reported in Table 1. The initial position of the spacecraft is assumed to be uncertain with standard deviations $3\sigma_x = 0.008$ and $3\sigma_y = 0.08$ on the x and y components of the position vector, with no correlation between the different components. The uncertain initial state is propagated forward to the final epoch $t_f = 0.95\,T$, where $T = 2\pi$ is the nominal period of the orbit. First of all, a Monte Carlo simulation is carried out to propagate 10^5

DOI: 10.13009/EUCASS2017-607

Table 1: Initial conditions in the 2BP.

x_0	y_0	z_0	$v_{x,0}$	$v_{y,0}$	$v_{z,0}$
1	0	0	0	$\sqrt{1+e}$	0

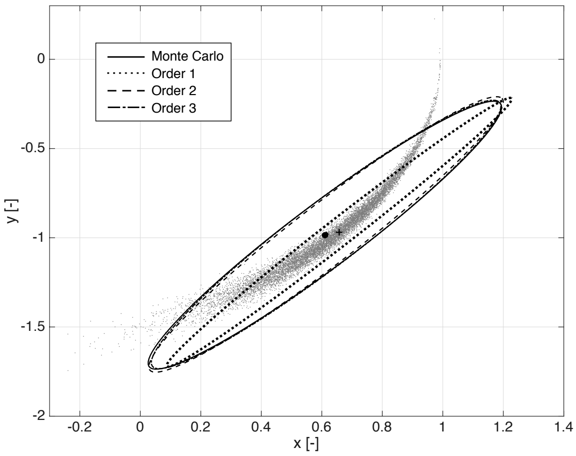

Figure 2: Propagated mean and covariance for the illustrative example on two-body dynamics: comparison between a Monte Carlo simulation and the DA-based estimation at different orders. Grey dots represent the propagated samples of the Monte Carlo simulation.

initial conditions to t_f and to compute the resulting mean and covariance, which are used as reference for the following analysis. As can be seen from Fig. 2, the samples of the Monte Carlo simulation at t_f exhibit an evident nonlinear distribution.

Using the techniques introduced in Sect. 2, DA is then used to compute arbitrary order Taylor expansions of the spacecraft state at t_f with respect to x_0 and y_0. The resulting polynomials are used to compute the propagated mean and covariance using the formulas of Eq. (6). Fig. 2 reports the results obtained for different expansion orders. As shown in the figure, the first order expansion fails to accurately estimate the exact mean and covariance, which are represented by the result of the Monte Carlo simulation. The second order expansion already introduces sufficient information for an accurate representation of both moments. The third order expansion do not provide further improvements in terms of accuracy. Thus, being based on a Gaussian representation of the propagated uncertainties, the accuracy of the extended Kalman filter significantly benefits of a second order expansion of the flow of the dynamics. However, no relevant improvement is obtained with higher orders.

Based on these results, the assessment of the performance of the DA-based HNEKF will be limited to the use of first and second order expansions in the following analyses.

4. Relative Pose Estimation

This paper focuses on exploiting the proposed DA-based HNEKF to face the challenging problem of estimating the spacecraft state for proximity operations during a rendezvous with an uncooperative target. In particular, the ESA e.deorbit mission[3] is considered as reference and Envisat is selected as target satellite.

In the following analysis, some assumptions are made. Firstly, an *a priori* knowledge of both chaser and target is assumed, i.e. the inertia properties are perfectly known. Secondly, the chaser motion is supposed to be deterministic and, thus the related data are not affected by noise and uncertainties. Finally, neither flexible dynamics nor external disturbances are considered. It should be noticed that neglecting external disturbances and flexibility implies the decoupling of the relative translational and rotational dynamics.

4.1 Relative translational dynamics

The relative translational dynamic equations are developed in the local vertical local horizontal (LVLH) frame fixed on the chaser. In this frame the target relative position $\boldsymbol{r}_r$ and velocity $\boldsymbol{v}_r$ can be defined as:

DOI: 10.13009/EUCASS2017-607

$$\boldsymbol{r}_r = x\hat{\boldsymbol{r}} + y\hat{\boldsymbol{\theta}} + z\hat{\boldsymbol{h}} \tag{8}$$

$$\boldsymbol{v}_r = \dot{x}\hat{\boldsymbol{r}} + \dot{y}\hat{\boldsymbol{\theta}} + \dot{z}\hat{\boldsymbol{h}} \tag{9}$$

where x, y and z are the three components of $\boldsymbol{r}_r$ in the chaser LVLH frame and $\hat{\boldsymbol{r}}$, $\hat{\boldsymbol{\theta}}$ and $\hat{\boldsymbol{h}}$ are the versors of the considered triad. The relative translational dynamics are governed by the following equations:[12]

$$\ddot{x} - 2\dot{\nu}\dot{y} - \ddot{\nu}y - \dot{\nu}^2 x = -\mu(\bar{r} + x)/[(\bar{r} + x)^2 + y^2 + z^2]^{3/2} + \mu/\bar{r}^2 \tag{10}$$

$$\ddot{y} + 2\dot{\nu}\dot{x} + \ddot{\nu}x - \dot{\nu}^2 y = -\mu y/[(\bar{r} + x)^2 + y^2 + z^2]^{3/2} \tag{11}$$

$$\ddot{z} = -\mu z/[(\bar{r} + x)^2 + y^2 + z^2]^{3/2} \tag{12}$$

where μ is the gravitational parameter, $\bar{r}$ is the distance from the Earth center to the chaser and ν is the true anomaly. Finally, the motion of the chaser is described by the following equations:

$$\ddot{\bar{r}} = \bar{r}\dot{\nu}^2 - \mu/\bar{r}^2 \tag{13}$$

$$\ddot{\nu} = -2\dot{\bar{r}}\dot{\nu}/\bar{r} \tag{14}$$

4.2 Relative rotational dynamics

As for the rotational dynamics, the relative orientation of the body-fixed reference frame on the target with respect to the body-fixed reference frame on the chaser can be described through a rotation matrix $\boldsymbol{\Gamma}$. Consequently, the relative angular velocity and acceleration of the target can be expressed as follows:

$$\boldsymbol{\omega}_r = \boldsymbol{\omega}_t - \boldsymbol{\Gamma}\boldsymbol{\omega}_c \tag{15}$$

$$\dot{\boldsymbol{\omega}}_r = \dot{\boldsymbol{\omega}}_t - \boldsymbol{\Gamma}\dot{\boldsymbol{\omega}}_c + \dot{\boldsymbol{\omega}}_{app} \tag{16}$$

$$\dot{\boldsymbol{\omega}}_{app} = \boldsymbol{\omega}_r \times \boldsymbol{\Gamma}\boldsymbol{\omega}_c \tag{17}$$

where $\boldsymbol{\omega}_c$ and $\boldsymbol{\omega}_t$ are the angular velocity of the chaser and the target expressed in their body-fixed reference frame, respectively, whereas $\boldsymbol{\omega}_r$ is the relative angular velocity expressed in the target body-fixed reference frame.

The relative attitude of the target can be described parameterizing the rotation matrix $\boldsymbol{\Gamma}$. To this aim, the Modified Rodrigues Parameters (MRP) are adopted in this study.[7] The MRP are related to quaternions and to the rotation matrix by the following relations:

$$\boldsymbol{\zeta} = \frac{\tilde{\boldsymbol{q}}}{1 + \boldsymbol{q}_0} \tag{18}$$

$$\boldsymbol{\Gamma}(\zeta) = \boldsymbol{I}_3 - \alpha_1^A[\zeta\times] + \alpha_2^A[\zeta\times]^2 \tag{19}$$

$$\begin{cases} \alpha_1^A = 4\frac{1-\boldsymbol{\zeta}^T\boldsymbol{\zeta}}{(1+\boldsymbol{\zeta}^T\boldsymbol{\zeta})^2} \\ \alpha_2^A = 8\frac{1}{(1+\boldsymbol{\zeta}^T\boldsymbol{\zeta})^2} \end{cases} \tag{20}$$

where $\boldsymbol{\zeta}$ are the MRP, $\tilde{\boldsymbol{q}}$ are the quaternions and $\boldsymbol{I}_3$ is the identity matrix.

The time evolution of the MRP is governed by Eq. 21.

$$\dot{\boldsymbol{\zeta}} = \frac{1}{4}\boldsymbol{\Sigma}(\zeta)\boldsymbol{\omega}_r \tag{21}$$

$$\boldsymbol{\Sigma}(\zeta) = (1 - \zeta^T\zeta)\boldsymbol{I}_3 + 2\zeta\zeta^T + 2[\zeta\times] \tag{22}$$

DOI: 10.13009/EUCASS2017-607

As for the dynamics, the chaser motion is described by the torque-free Euler equations, while the relative attitude dynamics can be obtained substituting kinematics relationship in the Euler absolute equations of the target spacecraft. The resulting dynamic system is:

$$\boldsymbol{J}_t\dot{\boldsymbol{\omega}}_r + \boldsymbol{\omega}_r \times \boldsymbol{J}_t\boldsymbol{\omega}_r = \boldsymbol{M}_{app} - \boldsymbol{M}_g - \boldsymbol{M}_{ci} \tag{23}$$

$$\boldsymbol{M}_{app} = \boldsymbol{J}_t\boldsymbol{\omega}_r \times \boldsymbol{\Gamma}\boldsymbol{\omega}_c \tag{24}$$

$$\boldsymbol{M}_{ci} = \boldsymbol{J}_t\boldsymbol{\Gamma}\dot{\boldsymbol{\omega}}_c \tag{25}$$

$$\boldsymbol{M}_g = \boldsymbol{M}_{gc} + \boldsymbol{M}_{gcoup} \tag{26}$$

$$\boldsymbol{M}_{gc} = \boldsymbol{\Gamma}\boldsymbol{\omega}_c \times \boldsymbol{J}_t\boldsymbol{\Gamma}\boldsymbol{\omega}_c \tag{27}$$

$$\boldsymbol{M}_{gcoup} = (\boldsymbol{\omega}_r \times \boldsymbol{J}_t\boldsymbol{\Gamma}\boldsymbol{\omega}_c + \boldsymbol{\Gamma}\boldsymbol{\omega}_c \times \boldsymbol{J}_t\boldsymbol{\omega}_r) \tag{28}$$

where $\boldsymbol{J}_t$ is the matrix of inertia of the target, $\boldsymbol{M}_{app}$ is the apparent torques, $\boldsymbol{M}_{ci}$ is the chaser-inertial torques and $\boldsymbol{M}_g$ is the gyroscopic torques.

4.3 Measurement model

In real application relative position and relative attitude measurements can be obtained by processing images from a camera. In this study, they are generated numerically exploiting a suitable error model.

While the relative position is already part of the state vector, and thus it is linearly related to it, the attitude is provided in terms of roll, pitch and yaw angles (hereinafter also referred to as ϕ, θ and ψ). Consequently, it is necessary to derive the rotation matrix $\boldsymbol{\Gamma}$ from the MRP (see Eq. (19)) and, afterwards compute the roll, pitch and yaw angles from the associated parameterization. The relations binding the MRP and the measured attitude introduce other nonlinearities in the problem.

For the measurements generation, the true states of the target spacecraft are computed through the integration of the dynamic equations (see Sect. 4.1-4.2) and then the related measured quantities are derived. Afterwards, some noise is introduced as an exponentially correlated random variable according to the following model:

$$E(t_{k+1}) = KE(t_k) + \sqrt{1-K^2} \cdot \mathcal{N}(0,\sigma) \tag{29}$$

$$K = exp(-1/(f\tau)) \tag{30}$$

where E is the error w.r.t. the true states, $\mathcal{N}(0,\sigma)$ is a random number generated with a normal distribution of zero mean and standard deviation σ, f is the measurement acquisition frequency and τ is the autocorrelation time. In this model, the error at time $k+1$ is exponentially correlated to the error at the previous instant, and this correlation decays with a time scale defined by τ. Considering a camera, this seems to be a more reasonable model w.r.t. the Gaussian one in which error values at different time instant are completely uncorrelated.

4.4 Software architecture

Fig. 3 reports the software architecture, which is made up of three main blocks. The first one is the "dynamics simulator+noise generator" that receives as inputs the initial states, then propagates the dynamics through a variable-step integrator (Runge-Kutta78) and generates the measurements adding noise computed with the exponentially correlated random model. These computations are performed in advance and the outputs are loaded in memory before running the filter.

For the filtering, the decoupling of the dynamics is exploited to split the problem into two parts: the estimation of the relative translational states ($\boldsymbol{r}_r$ and $\boldsymbol{v}_r$) and the estimation of the relative rotational states ($\boldsymbol{\zeta}$ and $\boldsymbol{\omega}_r$). In this way, 6 DA variables have to be initialized for each filter instead of 12, lightening the computational burden. In both filters the required measurements and chaser absolute state are loaded at the beginning and an initial estimate of the relative states, in terms of mean and covariance, has to be provided. For the relative dynamics propagation inside the

DOI: 10.13009/EUCASS2017-607

filter, a 4^{th}-order Runge-Kutta integrator is exploited since it is a better solution for embedded systems in terms of computational effort.

Finally, the estimated relative state is compared with the true state propagated by the dynamics simulator to assess the performance of the filters.

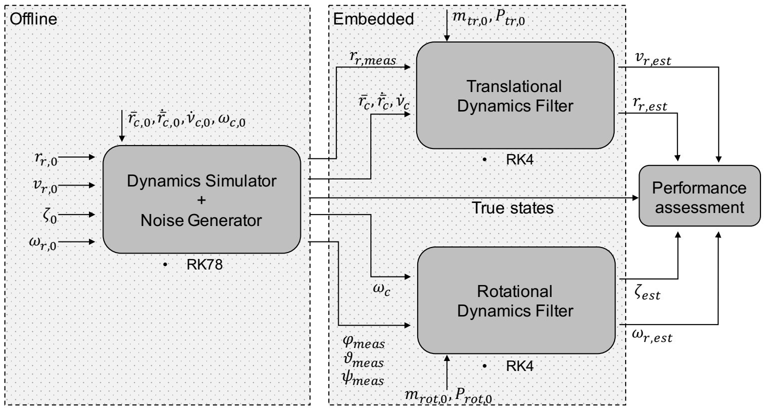

Figure 3: Software architecture.

5. Results

In the numerical analysis, the chaser and target are assumed to be on the same orbit at a reasonable distance for a proper functioning of the camera. The initial conditions of the relative states are reported in Table 2. The attitude is initialized randomly, while the angular velocity is selected in order to have an absolute value of about 2.5 deg/s.

In the following sections, first, the accuracy and robustness of the first and second order filter are assessed, and then an analysis on the required computational time is performed in order to verify the real-time feasibility.

Table 2: Initial conditions.

Tr. Dyn.		Rot. Dyn.	
x (m)	-0.002	ϕ (rad)	1.66
y (m)	-31.17	θ (rad)	2.27
z (m)	0	ψ (rad)	-0.38
$\dot{x}$ (m/s)	-3.5e-6	$\omega_{r,x}$ (rad/s)	0.02
$\dot{y}$ (m/s)	-2.0e-6	$\omega_{r,y}$ (rad/s)	0.02
$\dot{z}$ (m/s)	0	$\omega_{r,z}$ (rad/s)	0.04

5.1 Accuracy and robustness analysis

Before presenting the results, some comments are provided to guide the reader through the following analyses. First, the target velocity can be assumed to be the most uncertain variables since neither *a priori* knowledge nor direct measurements are available. Then, when limited-resource systems are considered, low measurement acquisition frequency could be imposed or at least beneficial. Therefore, a Monte Carlo-based sensitivity analysis is carried out to assess the robustness of the first and second order filter with various acquisition frequencies and initial uncertainty in the relative velocity. The examined cases are reported in Table 3, for the translational filter, and in Table 4, for the rotational filter, being $\sigma_{i,0}$ and σ_i^s the initial standard deviation and the sensor standard deviation, respectively, of the variable i.

DOI: 10.13009/EUCASS2017-607

Table 3: Translational dynamics: sensitivity to initial velocity uncertainty and acquisition frequency.

Dynamics		Sensors		Frequency
$\sigma_{r_r,0}$ (m)	1	$\sigma^s_{x,y}$ (m)	0.02	0.1 Hz to 3 Hz
$\sigma_{v_r,0}$ (m/s)	K*0.1	σ^s_z (m)	0.03	
K = [0.1,0.5,1,5,10]				

Table 4: Rotational dynamics: sensitivity to angular velocity uncertainty and acquisition frequency.

Dynamics		Sensors		Frequency
$\sigma_{\zeta,0}$ ()	0.02	$\sigma^s_{\phi,\theta}$ (rad)	0.003	0.1 Hz to 3 Hz
$\sigma_{\omega_r,0}$ (rad/s)	K*0.01	σ^s_ψ (rad)	0.006	
K = [0.1,0.5,1,5,10]				

For each case, 1000 samples are generated around the true initial conditions, according to the statistics, and then the furthest 100 are selected and used as initial estimate of the relative state in the filter. This choice is motivated by the will to study the worst circumstances, in which the nonlinearities are expected to play a prominent role.

Afterwards, the performance are quantified by means of some statistical indices, reported in Eqs. (31) and (32).

$$_n\bar{\mu} = \frac{\sum_{i=1}^{100} RMSE_i}{100} \tag{31}$$

$$_n\sigma_{\bar{\mu}} = \Big[\frac{\sum_{i=1}^{100}(_n\bar{\mu} - RMSE_i)^2}{100}\Big]^{\frac{1}{2}} \tag{32}$$

$RMSE_i$ is the root mean square error of the estimated variables computed at steady state for the i^{th} simulation, $_n\bar{\mu}$ and $_n\sigma_{\bar{\mu}}$ are the mean and the standard deviation of RMSE, respectively, considering the filter of order n. Fig. 4 provides a deeper insight of the indices: $\bar{\mu}$ gives the mean accuracy of the filter, while $\sigma_{\bar{\mu}}$ quantifies the dispersion around the mean. If the standard deviation is high, the final accuracy strongly depends on the estimate of the initial conditions and thus large initial errors may result in bad performance or even failure.

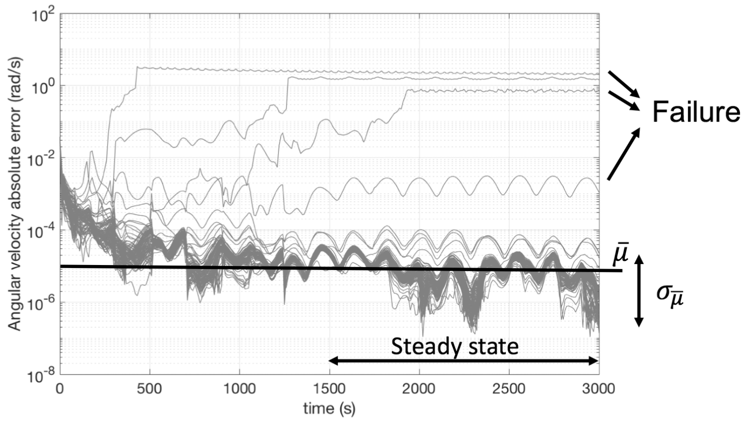

Figure 4: Graphical representation of the statistical indices.

5.1.1 Translational dynamics filter

The translational dynamics is almost static and linear since the two spacecrafts are very close on the same orbit, which is nearly circular. Therefore, high-order filters do not provide better performance w.r.t. a linear one, which is already capable of following the dynamic evolution. Indeed, both first and second order filters succeed in all the considered conditions of acquisition frequency and initial velocity uncertainty with the same estimation error at steady state, which

DOI: 10.13009/EUCASS2017-607

is in the order of 10^{-2} m for the position and 10^{-7} m/s for the velocity. As example, in Fig. 5 the absolute position and velocity errors considering a frequency of 3 Hz and $\sigma_{r_r,0}$ = 0.01 m/s are reported.

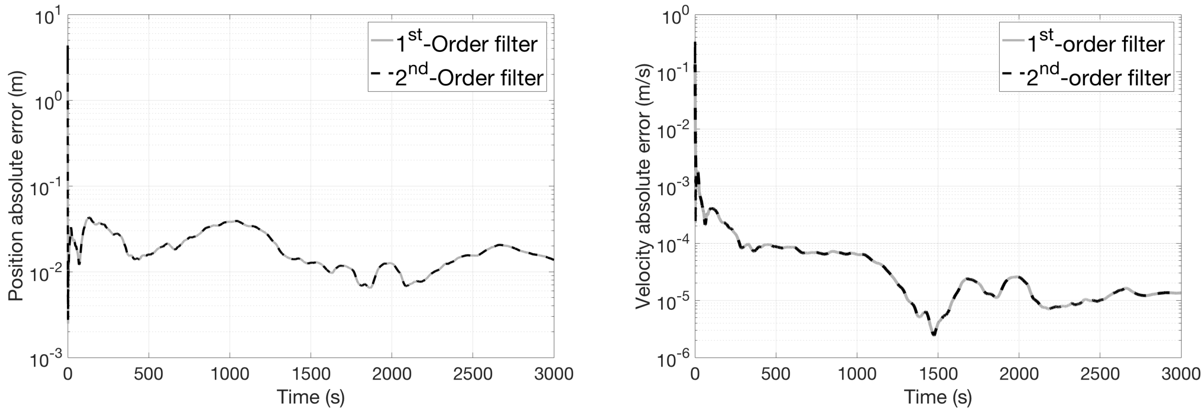

(a) (b)

Figure 5: Position (a) and velocity (b) absolute error with a frequency of 3 Hz and $\sigma_{r_r,0}$ = 0.01 m/s.

5.1.2 Rotational dynamics filter

Regarding the rotational dynamics filter, the nonlinearities affect the estimation more significantly, especially in case of high uncertainties and low observability of the system.

In order to compare the two filters and have a deeper insight into their performance, the ratios $\frac{_2\bar{\mu}}{_1\bar{\mu}}$ and $\frac{_2\sigma_{\bar{\mu}}}{_1\sigma_{\bar{\mu}}}$ are computed and reported in Tables 5-6. The superscript reports the success percentage (i.e., when the filter converges) of the second order filter, while the subscript the success percentage of the first order filter.

On one hand, it can be observed that first and second order filters present the same performance for low uncertainties and high frequency. However, moving to high uncertainties and low frequency (shaded area), the second order filter starts outperfoming the first order filter. Indeed, even though $_1\bar{\mu}$ is very similar to $_2\bar{\mu}$, $_1\sigma_{\bar{\mu}}$ is significantly larger than $_2\sigma_{\bar{\mu}}$, namely the first order filter features a higher dispersion of the steady-state estimation error. This means that, in case of large deviations from the true initial conditions, the first order filter performance deteriorate leading to final estimates up to 2 order of magnitude worse than the second order filter. For instance, Fig. 6 reports the MRP and angular velocity absolute error considering an acquisition frequency of 0.4 Hz, $\sigma_{\omega_r,0}$ = 0.05 rad/s and inaccurate initial estimate of the states.

Finally, the second order filter turns out to be also more robust in terms of failure. Indeed, in some cases, the fisrt order filter do not manage to deal with the nonlinearity and diverges, while the second order filter converges.

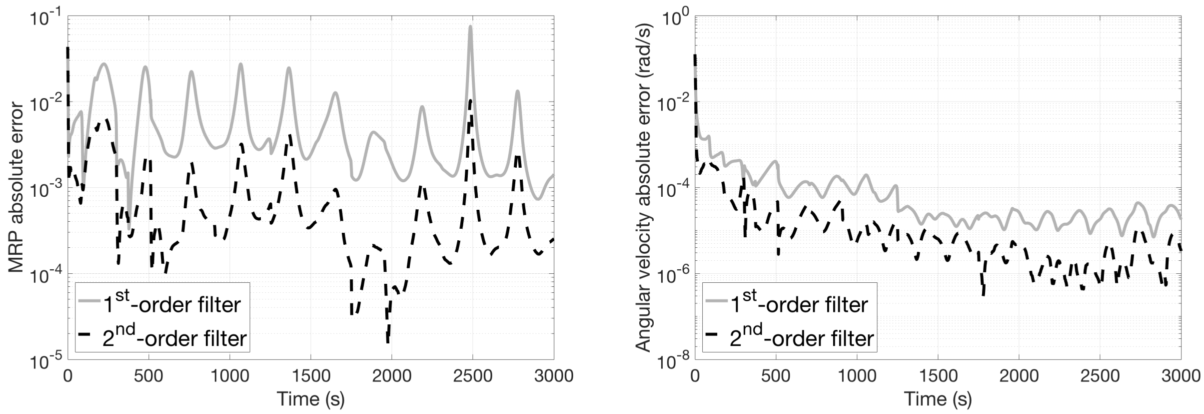

(a) (b)

Figure 6: MRP (a) and angular velocity (b) absolute error with a frequency of 0.4 Hz, $\sigma_{\omega_r,0}$ = 0.05 rad/s and inaccurate initial estimate.

DOI: 10.13009/EUCASS2017-607

Table 5: Ratio $\frac{{}_2\bar{\mu}}{{}_1\bar{\mu}}$ for the MRP (a) and the angular velocity (b).

Freq. (Hz)	$\sigma_{\omega_r,0}$ (rad/s) 0.001	0.005	0.01	0.05	0.1
0.1	0.995^{100}_{100}	0.991^{100}_{100}	0.882^{100}_{97}	0.373^{54}_{17}	$-^{0}_{0}$
0.4	0.997^{100}_{100}	0.997^{100}_{100}	0.997^{100}_{100}	0.790^{100}_{75}	0.759^{99}_{81}
1	0.999^{100}_{100}	0.998^{100}_{100}	0.999^{100}_{100}	0.998^{100}_{100}	0.993^{100}_{100}
3	1.000^{100}_{100}	1.000^{100}_{100}	1.000^{100}_{100}	1.000^{100}_{100}	1.000^{100}_{100}

(a)

Freq. (Hz)	$\sigma_{\omega_r,0}$ (rad/s) 0.001	0.005	0.01	0.05	0.1
0.1	0.999^{100}_{100}	0.999^{100}_{100}	0.985^{100}_{97}	0.421^{54}_{17}	$-^{0}_{0}$
0.4	0.999^{100}_{100}	0.999^{100}_{100}	0.999^{100}_{100}	0.757^{100}_{75}	0.798^{99}_{81}
1	0.999^{100}_{100}	0.999^{100}_{100}	0.999^{100}_{100}	0.999^{100}_{100}	0.997^{100}_{100}
3	1.000^{100}_{100}	1.000^{100}_{100}	1.000^{100}_{100}	1.000^{100}_{100}	1.000^{100}_{100}

(b)

Table 6: Ratio $\frac{{}_2\sigma_{\bar{\mu}}}{{}_1\sigma_{\bar{\mu}}}$ for the MRP (a) and the angular velocity (b).

Freq. (Hz)	$\sigma_{\omega_r,0}$ (rad/s) 0.001	0.005	0.01	0.05	0.1
0.1	0.688^{100}_{100}	0.386^{100}_{100}	0.009^{100}_{97}	0.359^{54}_{17}	$-^{0}_{0}$
0.4	0.782^{100}_{100}	0.752^{100}_{100}	0.669^{100}_{100}	0.003^{100}_{75}	0.015^{99}_{81}
1	0.795^{100}_{100}	0.791^{100}_{100}	0.778^{100}_{100}	0.435^{100}_{100}	0.060^{100}_{100}
3	0.797^{100}_{100}	0.797^{100}_{100}	0.799^{100}_{100}	0.771^{100}_{100}	0.645^{100}_{100}

(a)

Freq. (Hz)	$\sigma_{\omega_r,0}$ (rad/s) 0.001	0.005	0.01	0.05	0.1
0.1	0.839^{100}_{100}	0.522^{100}_{100}	0.048^{100}_{97}	0.306^{54}_{17}	$-^{0}_{0}$
0.4	0.830^{100}_{100}	0.803^{100}_{100}	0.721^{100}_{100}	0.004^{100}_{75}	0.019^{99}_{81}
1	0.788^{100}_{100}	0.783^{100}_{100}	0.771^{100}_{100}	0.421^{100}_{100}	0.382^{100}_{100}
3	0.821^{100}_{100}	0.807^{100}_{100}	0.804^{100}_{100}	0.755^{100}_{100}	0.687^{100}_{100}

(b)

DOI: 10.13009/EUCASS2017-607

5.2 Computational time on the BeagleBone Black

This section addresses the assessment of the required computational effort of the DA-based HNEKF on the BeagleBone Black (BBB) Single Board Computer, based on an ARMv7 processor (Cortex A8) @ 1GHz with 512Mb of RAM. The BBB is deemed to be representative of the limited computational capability available on onboard space processors. The filter is entirely compiled out of C11 code directly on the target ARM platform, which is running a tailored Linux 4.9 kernel and proper GCC compiler.

In order to asses the feasibility of the developed filter on the embedded hardware, a Real-Time Operative System (RTOS) should have been employed, allowing the real time scheduling of the filter task at the desired frequency. However, the filter does not really acquire measurements since those are generated in advance by the dynamics simulator. Therefore, an accurate real time scheduling is not strictly required. Indeed, the computational time required by each step of the filter can be measured and compared to the time step at the desired frequency, checking that it is smaller.

To this aim, the duty cycle concept is introduced. The duty cycle represent the fraction of the available sampling time which is used by the filter task, as shown in Fig. 7. Therefore, given the execution time t_{exec} and defining the sampling time as:

$$t_a = \frac{1}{f} \tag{33}$$

the duty cycle is:

$$DC = \frac{t_{exec}}{t_a} \tag{34}$$

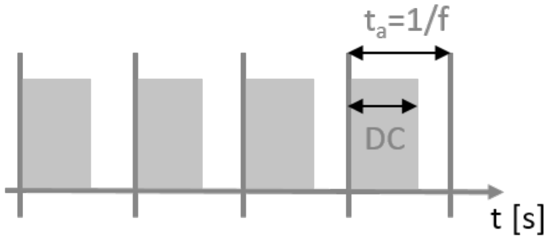

Figure 7: Duty cycle concept

The analysis is carried out considering different sampling frequency and processor clock frequency on the BBB. More specifically, the sampling frequencies are $f = [0.1, 0.4, 1, 3]$ Hz while the clock frequencies are $clk = [100^{*}, 275, 720, 1000]$ MHz (* Interpolated). First and second order filters are executed considering both the translational and rotational dynamics. The results of the execution time and duty cycle are reported in Table 7.

Table 7: Filter execution on BBB

Execution Time [s] - Order 1				
f\clk	100	275	720	1000
0.1	0.381	0.303	0.110	0.006
0.4	0.115	0.091	0.035	0.004
1	0.062	0.049	0.018	0.002
3	0.026	0.021	0.008	0.001

Duty Cycle [%] - Order 1				
f\clk	100	275	720	1000
0.1	3.8%	1.2%	0.1%	0.0%
0.4	4.6%	0.4%	0.0%	0.0%
1	6.2%	0.3%	0.0%	0.0%
3	7.8%	0.2%	0.0%	0.0%

Execution Time [s] - Order 2				
f\clk	100	275	720	1000
0.1	1.342	1.072	0.413	0.043
0.4	0.426	0.339	0.129	0.014
1	0.25	0.199	0.077	0.011
3	0.124	0.099	0.039	0.007

Duty Cycle [%] - Order 2				
f\clk	100	275	720	1000
0.1	13.4%	14.4%	5.9%	0.3%
0.4	17.0%	5.8%	0.7%	0.0%
1	25.0%	5.0%	0.4%	0.0%
3	37.2%	3.7%	0.1%	0.0%

It is clear that both first and second order filters are always feasible, as the duty cycle remains always well below the 50%, thus allowing for the filtering and also other necessary tasks. Not surprisingly, the duty cycle increases

DOI: 10.13009/EUCASS2017-607

when reducing the clock frequency as the processor is capable of executing less operation per seconds. Moreover, at constant clock frequency, the duty cycle reduces when reducing the sampling frequency, demonstrating that the longer propagation time span, needed for computing the expectations, is not highly influencing the overall computational time. Concentrating on the lower clock frequency, it is possible to see how the second order filter is more feasible at lower sampling frequencies, that are the cases in which this filter outperforms the first order version.

6. Conclusion

The work investigated the possibility and assessed the advantages of onboard 6DoF state estimation using DA techniques. The problem of real-time relative pose estimation during proximity operations has been considered as target application, using the e.deorbit mission with the target Envisat as reference scenario. To attain this goal, a DA-based HNEKF has been developed and implemented on a BeagleBone Black platform, which is deemed to be representative of the limited computational performance available on current onboard space processors. The results show that using orders greater than two does not improve the accuracy of the estimation provided by the Kalman filter, which has been proven to be related to the hypothesis of the filter that all random distributions are Gaussian and, then, completely described by their mean and covariance. In addition, the second order filter tends to outperform the classical first order counterpart either for relatively large initial errors and uncertainties, or for relatively low acquisition frequencies. Nevertheless, the second order filter outperforms its first order version in terms of final error dispersion and robustness to failure. Finally, the tests have demonstrated that the second order filter can be run on an ARM processor @ 100 MHz for the target application.

7. Acknowledgments

This work has been carried out in collaboration with the Advanced Concepts Team under the Ariadna study "Assessment of onboard DA state estimation for spacecraft relative navigation" (Contract No. 4000117860/16/NL/LF/as).

References

[1] M. Berz. The method of power series tracking for the mathematical description of beam dynamics. *Nuclear Instruments and Methods in Physics Research Section A: Accelerators, Spectrometers, Detectors and Associated Equipment*, 258(3):431–436, 1987.

[2] M. Berz. *Modern Map Methods in Particle Beam Physics*. Academic Press, 1999.

[3] R Biesbroek. The e.deorbit esa cdf study. *Proceedings of the SPIE*, 5088:20–30, 2003.

[4] L. Isserlis. On a formula for the product-moment coefficient of any order of a normal frequency distribution in any number of variables. *Biometrika*, 12, 1918.

[5] S.J. Julier and J.K. Uhlmann. Unscented filtering and nonlinear estimation. *Proceedings of the IEEE*, 92(3):401–422, 2004.

[6] S.J. Julier, J.K. Uhlmann, and H.F. Durrant-Whyte. A new approach for filtering nonlinear systems. *Proceedings of the IEEE*, 3:1628–1632, 1995.

[7] S.R. Marandi and V.J. Modi. A preferred coordinate system and the associated orientation representation in attitude dynamics. *Acta Astronautica*, 15(11):833–843, 1987.

[8] O. Montenbruck and G. Eberhard. *Satellite orbits: models, methods, and applications*. Springer Verlag, 2000.

[9] R.S. Park and D.J. Scheeres. Nonlinear mapping of gaussian statistics: theory and applications to spacecraft trajectory design. *Journal of Guidance Control and Dynamics*, 29(6):1367–1375, 2006.

[10] R.S. Park and D.J. Scheeres. Nonlinear semi-analytic methods for trajectory estimation. *Journal of Guidance Control and Dynamics*, 30(6):1668–1676, 2007.

[11] M. Rasotto, A. Morselli, A. Wittig, M. Massari, P. Di Lizia, R. Armellin, C.Y. Valles, and G. Ortega. Differential algebra space toolbox for nonlinear uncertainty propagation in space dynamics. *Proceedings of the 6th International Conference on Astrodynamics Tools and Techniques*, 2016.

DOI: 10.13009/EUCASS2017-607

[12] H. Schaub and J. L. Junkins. *Analytical mechanics of space systems*. Aiaa, 2003.

[13] M. Valli, R. Armellin, P. Di Lizia, and M. Lavagna. Nonlinear filtering methods for spacecraft navigation based on differential algebra. *Acta Astronautica*, 94:363–374, 2014.

[14] J.R. Wertz and R. Bell. Autonomous rendezvous and docking technologies: status and prospects. *Proceedings of the SPIE*, 5088:20–30, 2003.